20. M. Kuno, J. K. Lee, B. O. Dabbousi, F. V. Mikulec, M. G. Bawendi, *J. Chem. Phys.* **106**, 9869 (1997).
21. *Mat. Res. Soc. Symp. Proc.* **272**, 229 (1992).
22. D. L. Schultz *et al.*, *Am. Inst. Phys. Conf. Proc.* **394**, 683 (1997).
23. M. L. Steigerwald *et al.*, *J. Am. Chem. Soc.* **110**, 3046 (1998).
24. S. Behrens *et al.*, *Angew. Chem. Int. Ed. Engl.* **35**, 2215 (1996).
25. A. Van Calster, A. Vervaet, I. De Rycke, J. De Baets, *J. Cryst. Growth* **86**, 924, (1998).
26. G. J. Scilla, J. J. Wysocki, *J. Vac. Sci. Technol.* **18**, 37 (1981).
27. C. Reita, *Inf. Display* **2**, 10 (1993).
28. T. P. Brody, *ibid.*, p. 5.
29. J. M. Jacobson *et al.*, invited talk given at the annual meeting of the Materials Research Society, Session G, on 29 November 1999 in Boston, MA.

30. We thank M. Bawendi, D. Antoniadis, C. Leatherdale, J. Taylor, S. Griffith, B. Hubert, and the staff at the Microsystems Technology Laboratory (MTL) for helpful discussion; M. Frongillo for assistance with TEM; L. Shaw for assistance with XPS; and M. Strojwas for help in device probing. TFT test structures were fabricated at the MTL at MIT. This work made use of MRSEC Shared Facilities supported by NSF under award number DMR-9400334. Supported by Defense Advanced Research Project Agency contract DABT63-99-C-0033 and by the MIT Media Lab's Things That Think (TTT) consortium. B.A.R. is partially supported by a graduate research fellowship from Motorola; B.N. is partially supported by a graduate research fellowship from NSF.

18 June 1999; accepted 14 September 1999

Bidirectional Semiconductor Laser

Claire Gmachl,* Alessandro Tredicucci, Deborah L. Sivco, Albert L. Hutchinson, Federico Capasso, Alfred Y. Cho

A semiconductor laser capable of operating under both positive and negative bias voltage is reported. Its active region behaves functionally as two different laser materials, emitting different wavelengths, depending on the design, when biased with opposite polarities. This concept was used for the generation of two wavelengths (6.3 and 6.5 micrometers) in the midinfrared region of the spectrum from a single quantum cascade laser structure. The two wavelengths are excited independently of each other and separated in time. This may have considerable impact on various semiconductor laser applications including trace gas analysis in remote sensing applications with differential absorption spectroscopy.

Most optoelectronic semiconductor devices, such as conventional semiconductor lasers, light-emitting diodes, and solar cells, are bipolar; that is, they contain a combination of semiconductor layers doped with donor impurities (n-type doped) and with acceptor impurities (p-type doped). The resulting built-in electrostatic potential provides an inherent directionality to these devices and renders them functional for a specific voltage polarity. On the contrary, unipolar optoelectronic devices offer the possibility of bidirectional use. The invention and development of unipolar lasers known as quantum cascade (QC) lasers (*1, 2*) have attracted considerable attention because they can be designed to operate in an extremely broad spectral range (the entire midinfrared spectrum). This is done by controlling the layer thicknesses rather than the material composition, with band-structure engineering (*3*) and molecular beam epitaxy (*4*). In addition, the generation of many laser photons per injected electron above threshold, due to the cascading of active regions, is responsible for the unprecedented power of QC lasers (*2, 5*).

Here, a bidirectional, unipolar semiconductor laser is presented. Unlike all other semiconductor lasers, including QC lasers fabricated to date (*2*), it operates as a light source under both positive and negative bias voltage. In addition, the operating wavelength can be made different in the two polarities. These features provide functionality not available in conventional semiconductor lasers, opening the door to many useful applications (*6*).

In QC lasers, the optical transition takes place between quantized states in the conduction band of a multiple quantum well structure (*1, 2*). The emission wavelength is determined by the energy level difference, which is controlled by the well and barrier thickness and the applied electric field. In general, reversing the applied bias in standard QC lasers alters the energy level structure, thus preventing laser action. The device presented in this paper operates instead as a different QC laser in each polarity.

In the diagram describing the basic principle of operation of the bidirectional QC laser (Fig. 1), a portion of the conduction band structure, two active regions with the connecting injector region, is shown. QC lasers typically contain a stack of $N \sim 30$ periods of alternating active regions and injectors (*2, 5*). In the present design, under an appropriate applied positive bias (Fig. 1A), laser action takes place from level G_+ to level 1, through a photon-assisted tunneling or diagonal transition (wavy arrow) because the two states have reduced spatial overlap (*7*). Level 1 is the ground state of the active region quantum well, whereas G_+ is the ground state of the miniband—a dense manifold of electronic levels in the superlattice injector. This miniband is designed so that under application of a suitable electric field, G_+ is spatially localized close to the injection barrier (*7*). The emitted photon energy is controlled, for a given active region quantum well, by the thickness of the injector layers in the immediate vicinity of the injection barrier and by the applied electric field. A reversal of the bias polarity (Fig. 1B) will localize the injector ground state G_- at the opposite end of the injector miniband. With an injector entirely symmetric around its center, G_+ and G_- would be equivalent, and the laser wavelength would be the same in both polarities. If, however, the injector regions are designed as asymmetric, the energy position of G_- will be different than that of G_+, leading to different laser wavelengths $\lambda_\pm$.

The exact layer design, a portion of the band structure, and the moduli squared of the relevant wave functions of sample D2520 are shown in Fig. 2. We briefly discuss the design parameters that are important for bidirectional, dual-wavelength operation. An in-depth description of QC lasers based on photon-assisted tunneling, including the implications of the reduced spatial overlap of the electron wave functions involved in laser action, can be found in (*7*). The important quantity in the calculation of the threshold gain of QC lasers is $k_\pm = z_\pm{}^2 E_\pm \tau_\pm$. The product of the first two factors, that is, the square of the optical matrix element $z_\pm$ and the energy of the transition $E_\pm$, is proportional to the oscillator strength $f_\pm$. $\tau_\pm$ is the lifetime of level $G_\pm$, determined mainly by the relaxation time from $G_\pm$ to level 1, due to the emission of a longitudinal optical phonon. The indices imply that these values can be set independently for each bias direction. If one is interested in a device with two different emission wavelengths, that is, $E_+ \neq E_-$, but comparable threshold current and voltage (*8*), then $z_\pm$ and $\tau_\pm$ need adjustment to achieve $k_- = k_+$ at the same applied electric field, regardless of the polarity.

For sample D2520, shown in Fig. 2 under an electric field of ±90 kV cm^{-1} corresponding to the threshold, we calculated $z_+ = 0.35$ nm, $z_- = 0.32$ nm, $\tau_+ = 46$ ps, $\tau_- = 64$ ps, and $E_+ = 198$ meV, $E_- = 173$ meV, respectively. This results in $k_+ = 1.12$ nm^2 ps eV and $k_- = 1.14$ nm^2 ps eV, which are sufficiently close to each other to suggest very similar threshold currents. Population

---

Bell Laboratories, Lucent Technologies, 600 Mountain Avenue, Murray Hill, NJ 07974, USA.

*To whom correspondence should be addressed. E-mail: cg@lucent.com

inversion necessary for laser action is guaranteed by the long lifetimes $\tau_\pm$ between the upper and lower laser levels, due to the relatively large spatial separation of the states ($G_\pm$ and 1) of the diagonal laser transition. In comparison, the time for electrons to tunnel resonantly from level 1 into a state of the injector region is calculated as 0.5 ps; the lifetime of $G_\pm$ due to the combined longitudinal optical phonon scattering rates into all states of the following, downstream injector region is ~380 ps.

The gain coefficient, defined as the quantity that multiplied by the current density J gives the peak material gain, is given by $g_\pm = (2e)/[\varepsilon_0 \hbar c L_p n_{\mathrm{eff}}(2\gamma)]k_\pm$ under the somewhat simplified assumption that the entire current passes through levels $G_\pm$ and 1 (*1*). $L_p = 35.4$ nm is the length of one stage (one active region plus injector), e is the unit charge, ε_0 is the vacuum dielectric constant, $\hbar$ is the reduced Planck's constant, c is the vacuum speed of light, $n_{\mathrm{eff}} = 3.26$ is the effective refractive index of the waveguide, and $2\gamma \approx 35$ meV is the luminescence linewidth. The latter was measured from subthreshold emission spectra. Inserting the above values into the equation for the gain coefficient results in $g_+ \approx g_- \approx 32$ cm kA^{-1}. This value is of the same order of magnitude as previously optimized unidirectional QC lasers (*7, 9, 10*), that is, QC lasers designed to operate solely under one bias polarity.

Other factors have to be considered in the design of bidirectional lasers. First, in a diagonal-transition QC laser, the transition matrix element and photon energy vary noticeably with the applied electric field (*7*) until laser threshold is reached. This variation with applied bias has to be taken into account when $z_\pm$ and $\tau_\pm$ are scaled to account for the desired difference in photon energy $E_\pm$ between opposite polarities.

Second, although one would expect the losses to be independent of bias polarity, the respective design in either polarity has to be analyzed to avoid an accidental resonant intersubband optical absorption.

Third, the injector regions are doped in their center wells and barriers, which for sample D2520 amounts to a sheet density of 3.5×10^{11} cm^{-2}. In general, the extrinsic electrons and the electrical potential of their donor ions will modify the band structure (*11*). We verified that this effect is negligible through self-consistent calculations of the band structure including the extrinsic charges and through measurements on two symmetric, bidirectional QC laser samples (D2488 and D2498) featuring doping profiles intentionally offset with respect to each other.

Finally, the waveguide cladding layers, their interfaces, and electrical contacts need to be equally functional in both bias directions. We confirmed this using sample D2453 with identical cladding, buffer, and contact layers but without active regions and injectors (*5*). The current-voltage (*I-V*) characteristics in both polarities were equal within a few percent.

All of the bidirectional laser samples contain a cascade of 36 active regions alternated with electron injectors. This stack is embedded in a dielectric waveguide very similar to those previously used with QC lasers (*5, 12*). We estimated a waveguide loss of $\alpha_w \approx 20$ cm^{-1}. The lasers are processed as conventional deep-etched ridge waveguide lasers (*5*) with stripe widths ranging from 10 to 20 μm. They are cleaved into bars with a length of ~3 mm, and the facets are left uncoated, which results in an outcoupling (mirror) loss of $\alpha_m \approx 4.2$ cm^{-1}.

Individual lasers are wire-bonded, soldered to a copper heat sink, and mounted on the temperature-controlled cold finger of a helium flow cryostat. The lasers are operated in pulsed mode with 50-ns-long current pulses in a low (5 to 100 kHz) repetition rate. The light is detected with a fast room temperature HgCdTe detector. Spectral measurements are performed with a Nicolet Fourier transform infrared spectrometer.

The device characteristics of a representative laser from wafer D2520 are displayed in Fig. 3. Figure 3A shows the emission wavelength as a function of the heat-sink temperature for both polarities. The two wavelengths at low temperature are $\lambda_- \approx 6.5$ μm and $\lambda_+ \approx 6.33$ μm. These wavelengths, although clearly distinct from each other, are closer than the design wavelengths $\lambda_- \approx 7.17$ μm and $\lambda_+ \approx 6.25$ μm. This discrepancy can easily be accounted for by noting that the transition energy is Stark-shifted in a linear fashion by a variation of the applied electric field and that the device has a higher laser threshold voltage under negative bias (Fig. 3B) (*13*). Here, the voltage (V) versus drive current (I) characteristics are shown at 20 K and the light-output power (L) versus I characteristics at several heat-sink temperatures. The *L-I-V* curves for both polarities are very similar in shape and values, with low-temperature threshold current densities $J_{\mathrm{th}} \approx 3.5$ kA cm^{-2}. This result should be compared with the calculated threshold of $J_{\mathrm{th}} = (g_\pm \Gamma)/(\alpha_m + \alpha_w) \approx 1.7$ kA cm^{-2}, with the values of $g_\pm$, α_w, and α_m given above and Γ, the mode confinement factor, being 0.45. We believe the difference between the measured and calculated values of J_{th} to be due to a decreased injection efficiency into the levels of the laser transition. Electrons can tunnel from the injector region into the first excited state 2 of the active region quantum well (Fig. 2). From there, electrons either tunnel into the

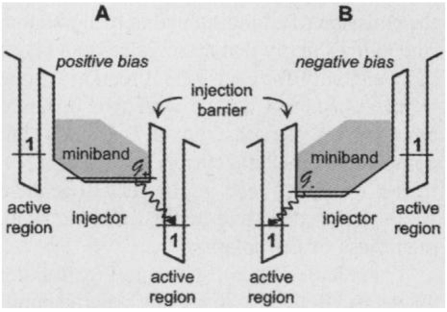

Fig. 1. Schematic energy diagram for the operation of the bidirectional QC laser. (**A**) A portion of the conduction band structure is shown under a positive applied bias. Electrons traverse the structure from left to right. (**B**) Schematic band structure of the same QC laser under opposite (negative) bias. Electrons traverse the structure from the opposite direction.

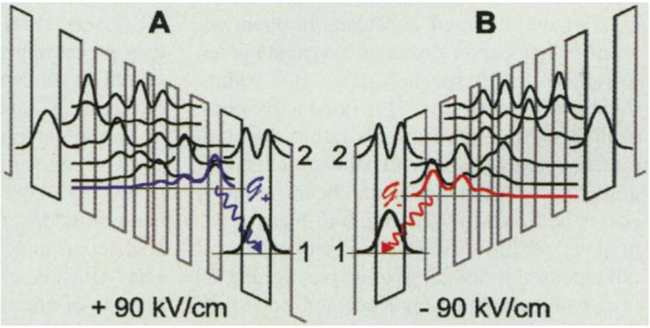

Fig. 2. Conduction band structure of a portion of sample D2520, a bidirectional QC laser with an emission wavelength dependent on bias polarity: (**A**) under a positive applied electric field of 90 kV cm^{-1}, approximately corresponding to laser threshold, and (**B**) under a negative applied electric field of the same magnitude. The actual layer thicknesses (in nanometers) are from left to right for both (A) and (B), starting from the first injection barrier: **3.5**/4.8/**3.5**/*2.4*/***2.5***/*2.6*/***1.5***/*2.2*/***1.0***/*2.2*/***1.9***/*2.2*/***2.9***/*2.2*/**3.5**/4.8/**3.5**. The $Al_{0.48}In_{0.52}As$ layers (energy barriers) are in bold symbols alternated with the $Ga_{0.47}In_{0.53}As$ wells. The underlined layers are doped to $n = 4 \times 10^{17}$ cm^{-3}; italics indicate the injector region. The moduli squared of the wave functions in the active and injector regions are shown. The blue wavy arrow indicates the laser transition for the positive polarity case (A), and the red wavy arrow indicates the laser transition for negative polarity (B). Not shown in Fig. 2, but structurally similar, are samples D2488 and D2498, two symmetric bidirectional QC lasers, designed to operate at the same wavelength under opposite bias polarity. The layer sequences are **3.5**/4.8/**3.5**/*2.4*/***2.5***/*2.6*/***1.5***/*2.2*/***1.0***/*2.2*/***1.5***/*2.6*/***2.5***/*2.4*/**3.5**/4.8/**3.5** ($n = 3 \times 10^{17}$ cm^{-3}) and **3.5**/4.8/**3.5**/*2.4*/***2.5***/*2.6*/***1.5***/*2.2*/***1.0***/*2.2*/***1.5***/*2.6*/***2.5***/*2.4*/**3.5**/4.8/**3.5** ($n = 4 \times 10^{17}$ cm^{-3}) for D2488 and D2498, respectively, with the same notation as sample D2520.

continuum region of the conduction band or scatter into the active region ground state. Both paths are deleterious for laser action, as they reduce the lifetime $\tau_\pm$ of state $G_\pm$ and in the latter case also temporarily add an electron to the lower laser level. This, in turn, leads to a reduced gain and a weaker inversion than previously estimated. We identified this process as the main source for the increased laser threshold using subthreshold luminescence spectra. A clear emission peak around 254 meV, in good agreement with the energy separation between the two states of the active region quantum well, indicates considerable electron population of its excited state. Nevertheless, the lasers display an optical peak output power of >100 mW and a slope efficiency (that is, an increase in optical power per unit current above threshold) of >120 mW A^{-1}.

Before fabricating the asymmetric device, we tested the idea of bidirectionality on a symmetric structure. This allowed us to verify that QC lasers can, in fact, be equally operated in both bias directions and with arbitrarily close emission wavelength. The latter is generally impossible for other multiple-wavelength semiconductor light sources because of mutual absorption or unsustainable oscillator strength partitioning between the two transitions (*14*).

The layer structure of the symmetric bidirectional laser samples (D2488 and D2498) is discussed in the caption of Fig. 2. At an applied electric field of ±90 kV cm^{-1}, we calculated values of $z_\pm = 0.29$ nm, $\tau_\pm = 75$ ps, and $E_\pm = 174$ meV ($\lambda_\pm = 7.15$ μm), which results in $k_\pm = 1.12$ nm^2 ps^{-1} eV^{-1} and in a gain coefficient $g_\pm \approx 32$ cm kA^{-1}.

The device characteristics of laser sample D2488 (Fig. 4) shows that both bias polarities result in emission at the same wavelength, $\lambda_\pm \approx 6.75$ μm, at cryogenic temperatures. The blue shift of the emission with increasing heat-sink temperature is caused by the larger threshold bias that must be applied to inject the correspondingly higher current density J_{th}. The laser shows a good threshold current density of ~3.1 kA cm^{-2} (see Fig. 4B). Peak optical powers of ≤300 mW are achieved at cryogenic temperatures, as well as a maximum slope efficiency of ≤480 mW A^{-1}. The latter value is excellent, even in comparison with some of the best unidirectional QC lasers published so far (*7, 9, 10*) with comparable wavelengths. The maximum pulsed operating temperature at present is ~150 K. This comparatively rapid decrease in device performance with heat-sink temperature is attributed to a thermal excitation of carriers into the excited state of the active region quantum well.

Besides other applications, this laser could provide an alternative to the use of two lasers, one in resonance with a particular molecular or atomic transition of a trace gas species and the other off resonance, in differential absorption LIDAR (light detection and ranging), also known as DIAL (*15, 16*). For this application, the laser would be operated by alternating current pulses of opposite polarity (or a sinusoidal current modulation), and the return signals at the two wavelengths would be ratioed. Finally, we note that the design principle of this laser is also applicable to interband cascade lasers with type II heterostructures (*17, 18*).

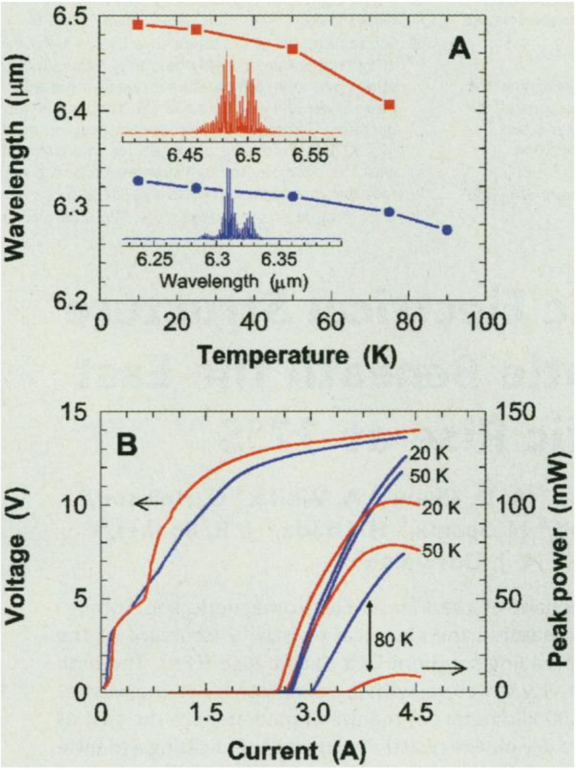

Fig. 3. Device characteristics of sample D2520, a bidirectional QC laser with two different emission wavelengths for opposite bias polarities. **(A)** The peak emission wavelength is shown as a function of the heat-sink temperature for positive (blue) and negative (red) polarity. The insets show examples of the corresponding emission spectra. The equally spaced peaks are the longitudinal modes of the optical cavity defined by the cleaved facets of the laser stripe. **(B)** Light output (*L*)–current (*I*) and current-voltage (*V*) characteristics of a 3-mm-long and 17-μm-wide, deep-etched, ridge waveguide laser operated in pulsed mode. The *I-V* characteristic has been measured at 20 K. *L-I* curves are shown at temperatures as indicated in the graph. Blue lines denote positive polarity and red lines negative polarity. The optical power is measured from a single facet with 60% collection efficiency.

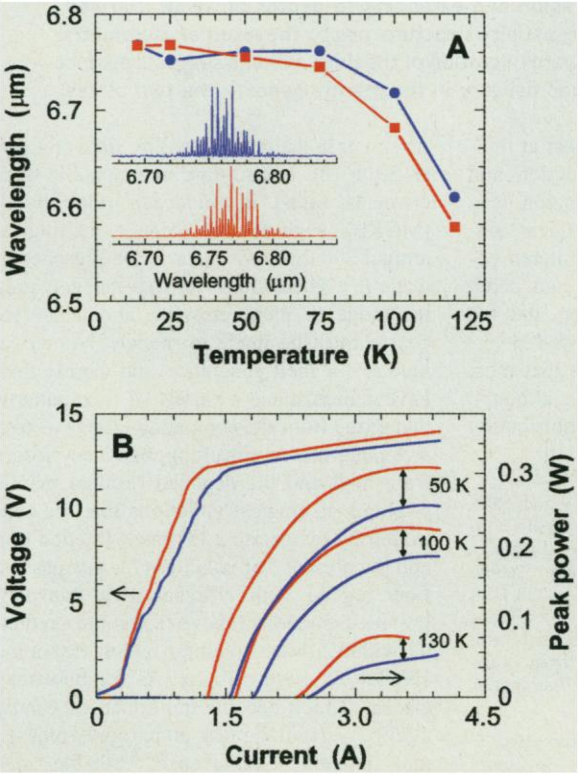

Fig. 4. Device characteristics of sample D2488, a symmetric bidirectional QC laser. **(A)** The peak emission wavelength is shown as a function of the heat-sink temperature for positive (blue) and negative (red) polarity. The insets are the corresponding emission spectra at low temperatures. The lack of a smooth envelop for all the Fabry-Perot modes is due to the overlap of the emission spectrum with the main absorption bands of water vapor in the beam path. **(B)** *L-I* and *I-V* characteristics of a 3-mm-long and 16-μm-wide, deep-etched, ridge waveguide laser operated in pulsed mode. The *I-V* characteristic has been measured at 50 K. *L-I* curves are shown at temperatures as indicated in the graph. Blue lines refer to positive polarity and red lines to negative polarity. The optical power is measured from a single facet with 60% collection efficiency.

References and Notes

1. J. Faist *et al.*, *Science* **264**, 553 (1994).
2. F. Capasso, C. Gmachl, D. L. Sivco, A. Y. Cho, *Phys. World* **12**, 27 (1999).
3. F. Capasso, *Science* **235**, 172 (1987).
4. A. Y. Cho Ed., *Molecular Beam Epitaxy* (AIP Press, Woodbury, NY, 1994).
5. C. Gmachl *et al.*, *IEEE J. Select. Topics Quantum Electron.*, **5**, 808 (1999).
6. Certain bipolar semiconductor lasers, when biased in reverse polarity, can function as photodetectors, as has recently been demonstrated (*19*).
7. J. Faist *et al.*, *Nature* **387**, 777 (1997).
8. This requirement makes the task of designing the bidirectional laser more difficult, as in general the applied electric field across any QC laser scales linearly with the energy of the optical transition.
9. J. Faist *et al.*, *Appl. Phys. Lett.* **68**, 3680 (1996).
10. J. Faist *et al.*, *IEEE J. Quantum Electron.* **34**, 336 (1998).
11. A. Tredicucci *et al.*, *Appl. Phys. Lett.* **72**, 2388 (1998).
12. C. Sirtori *et al.*, *ibid.* **66**, 3242 (1995).
13. The discrepancy in λ_+ (λ_-) corresponds to an applied bias 0.09 V (0.64 V) higher than the design value, which results in a relative difference in the threshold voltage of only 0.55 V. This is in reasonable agreement with the experiment and its uncertainties.
14. A. Tredicucci *et al.*, *Nature* **396**, 350 (1998), and references (*3*–*7*) therein.
15. M. W. Sigrist, *Air Monitoring by Spectroscopic Techniques* (Wiley, New York, 1994), chap. 3 and 5.
16. For applications of QC lasers in general, a high operating temperature is highly desirable. Although operation up to room temperature is readily achieved in a pulsed, low–duty-cycle mode (*5*), continuous wave operation is at present limited to temperatures below 175 K (*20*). Promising proposals for improvements exist, for example, through suppression of the nonradiative recombination pathways (*21*, *22*).
17. B. H. Yang *et al.*, *Appl. Phys. Lett.* **72**, 2220 (1998).
18. L. Olafsen *et al.*, *ibid.*, p. 2370.
19. D. A. Louderback, O. Sjölund, E. R. Hegblom, J. Ko, L. A. Coldren, *IEEE Photonics Technol. Lett.* **11**, 304 (1999).
20. C. Gmachl *et al.*, *ibid.*, in press.
21. C. F. Hsu, J. S. O, P. S. Zory, D. Botez, *Proc. SPIE* **3001**, 271 (1997).
22. K. W. Berryman, S. A. Lyon, M. Segev, J. R. Engholm, in *IEEE/OSA CLEO'99 Conference* (Optical Society of America, Washington, DC, 1999), p. 52.
23. We are grateful to S. N. G. Chu for his help with material characterization, in particular transmission electron microscopy, and to H. Kogelnik for stimulating discussions. This work has been supported in part by the Defense Advanced Research Projects Agency/U.S. Army Research Office under contract DAAG55-98-C-0050.

18 June 1999; accepted 15 September 1999

Asymmetric Electrical Structure in the Mantle Beneath the East Pacific Rise at 17°S

**R. L. Evans,[1]* P. Tarits,[2] A. D. Chave,[1] A. White,[3] G. Heinson,[3]
J. H. Filloux,[4] H. Toh,[5] N. Seama,[6] H. Utada,[7] J. R. Booker,[8]
M. J. Unsworth[8]**

The magnetotelluric component of the Mantle Electromagnetic and Tomography (MELT) Experiment measured the electrical resistivity structure of the mantle beneath the fast-spreading southern East Pacific Rise (EPR). The data reveal an asymmetric resistivity structure, with lower resistivity to the west of the ridge. The uppermost 100 kilometers of mantle immediately to the east of the ridge is consistent with a dry olivine resistivity structure indicating a mantle depleted of melt and volatiles. Mantle resistivities to the west of the ridge are consistent with a low-melt fraction (about 1 to 2 percent interconnected melt) distributed over a broad region and extending to depths of about 150 kilometers. The asymmetry in resistivity structure may be the result of asymmetric spreading rates and a westward migration of the ridge axis and suggests distinct styles of melt formation and delivery in the mantle beneath the two plates.

The generation of new oceanic crust at mid-ocean ridges involves the production and transport of melt from a source region deep within the mantle and its subsequent emplacement over a narrow zone centered beneath the ridge axis. The lateral and depth extents of the melt source region and the mode of melt delivery are not well determined. Geochemical data indicate that most melting occurs above 60 km (*1*), although there have been suggestions of a contribution from within the garnet stability field at greater depth (*2*). In addition, incompatible trace elements found in midocean ridge basalt (MORB) suggest that deeper melting at around 200 km may occur in the presence of water (*3*). There are fewer data that constrain the mode of melt transport, and hence recourse must be made to models. Numerical models for melt generation and mantle flow have demonstrated a variety of flow patterns that ensue from the competing effects of passive plate-driven upwelling, buoyancy forces from melt and the depleted residual mantle (*4*), and rheological variations that are controlled by temperature (*5*), melt fraction (*6*), and the presence of volatiles (*7*). In a passive flow regime with efficient melt transport, low-melt fractions (above 0.3%) are predicted within a broad melting region extending 100 km or more off-axis. As the buoyancy effects of melt become important, especially at lower spreading rates, more tightly focused melt delivery is achieved beneath the ridge with a depleted residual mantle produced just off-axis (*5*). Additionally, models that incorporate deeper incipient melting have been proposed with upwelling beginning at around 200-km depth and delivery of a small melt fraction to the ridge crest as part of a small-scale convective flow with a 200-km-length scale (*5*).

The MELT geophysical experiment (*8*), carried out at 17°S on the EPR, used seismic and electromagnetic observations to determine the geometry of the region of partial melting and the pattern of upwelling beneath a ridge, elucidate the melt concentration within that region, and determine the distribution and connectedness of melt in the rock matrix. The EPR near 17°S was chosen as the site for the MELT Experiment based on its fast (~150 mm/year) spreading rate and linear ridge morphology which, based on numerical models, was expected to maximize the two-dimensionality of mantle flow. However, the ridge has been shown to exhibit asymmetric spreading, with faster absolute plate motion on the Pacific plate resulting in a slow westward migration of the ridge axis with respect to the hot-spot reference frame. This asymmetry is manifest as lower subsidence of the sea floor with distance from the ridge to the west than to the east, and a greater abundance of seamounts on the Pacific plate than on the Nazca plate (*9*, *10*). The seismic component of MELT was completed in 1996 (*11*–*15*), and a key result from those analyses is that melt generation and transport occur over a broad region of the mantle, with no evidence found for a narrow column of melt beneath the ridge that would indicate highly focused melt delivery. Asymmetry between the eastern and western sides of the ridge is seen (*12*), with a zone of 1 to 2% melt inferred in the top 100 km of mantle extending some 300 to 400 km to the west of the ridge but only 150 km to the east (*11*–*13*). Reduced shear-wave velocities extend to depths in excess of 100 km, with a steep gradient in velocity between 100 and 180 km (*14*).

Here, we present initial results from the

---

[1] Woods Hole Oceanographic Institution, Woods Hole, MA 02543, USA. [2] UMR CNRS 6538, Universite Bretagne Occidentale, Brest, France. [3] Flinders University, Adelaide, South Australia 5042, Australia. [4] Scripps Institution of Oceanography, La Jolla, CA 92093, USA. [5] Toyama University, Toyama 930-8555, Japan. [6] Chiba University, Chiba, Japan. [7] Earthquake Research Institute, University of Tokyo, Tokyo 113, Japan. [8] Geophysics Program AK-50, University of Washington, Seattle, WA 98195, USA.

*To whom correspondence should be addressed. E-mail: revans@whoi.edu

LINKED CITATIONS

- Page 1 of 1 -

You have printed the following article:

Bidirectional Semiconductor Laser

Claire Gmachl; Alessandro Tredicucci; Deborah L. Sivco; Albert L. Hutchinson; Federico Capasso; Alfred Y. Cho

Science, New Series, Vol. 286, No. 5440. (Oct. 22, 1999), pp. 749-752.

Stable URL:

http://links.jstor.org/sici?sici=0036-8075%2819991022%293%3A286%3A5440%3C749%3ABSL%3E2.0.CO%3B2-R

This article references the following linked citations:

References and Notes

[1] **Quantum Cascade Laser**

Jerome Faist; Federico Capasso; Deborah L. Sivco; Carlo Sirtori; Albert L. Hutchinson; Alfred Y. Cho

Science, New Series, Vol. 264, No. 5158. (Apr. 22, 1994), pp. 553-556.

Stable URL:

http://links.jstor.org/sici?sici=0036-8075%2819940422%293%3A264%3A5158%3C553%3AQCL%3E2.0.CO%3B2-H

[3] **Band-Gap Engineering: From Physics and Materials to New Semiconductor Devices**

Federico Capasso

Science, New Series, Vol. 235, No. 4785. (Jan. 9, 1987), pp. 172-176.

Stable URL:

http://links.jstor.org/sici?sici=0036-8075%2819870109%293%3A235%3A4785%3C172%3ABEFPAM%3E2.0.CO%3B2-R

NOTE: *The reference numbering from the original has been maintained in this citation list.*